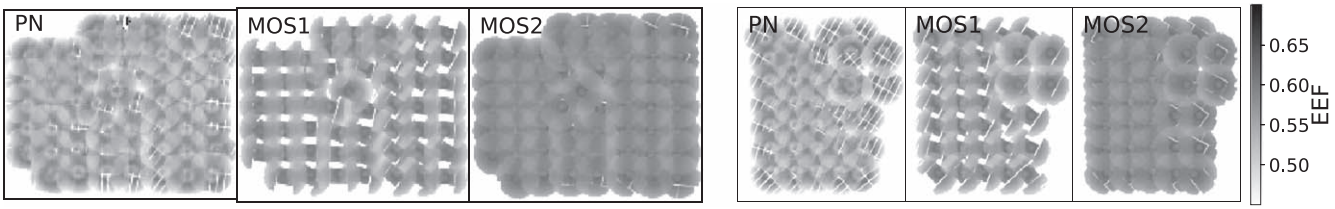

Figure 10. Soft-band encircled energy fraction (in 5 × 5 pixels) maps for the three EPIC cameras in W-CDF-S (left) and ELAIS-S1 (right). The gaps in the EEF map of MOS1 are due to its lost CCDs.

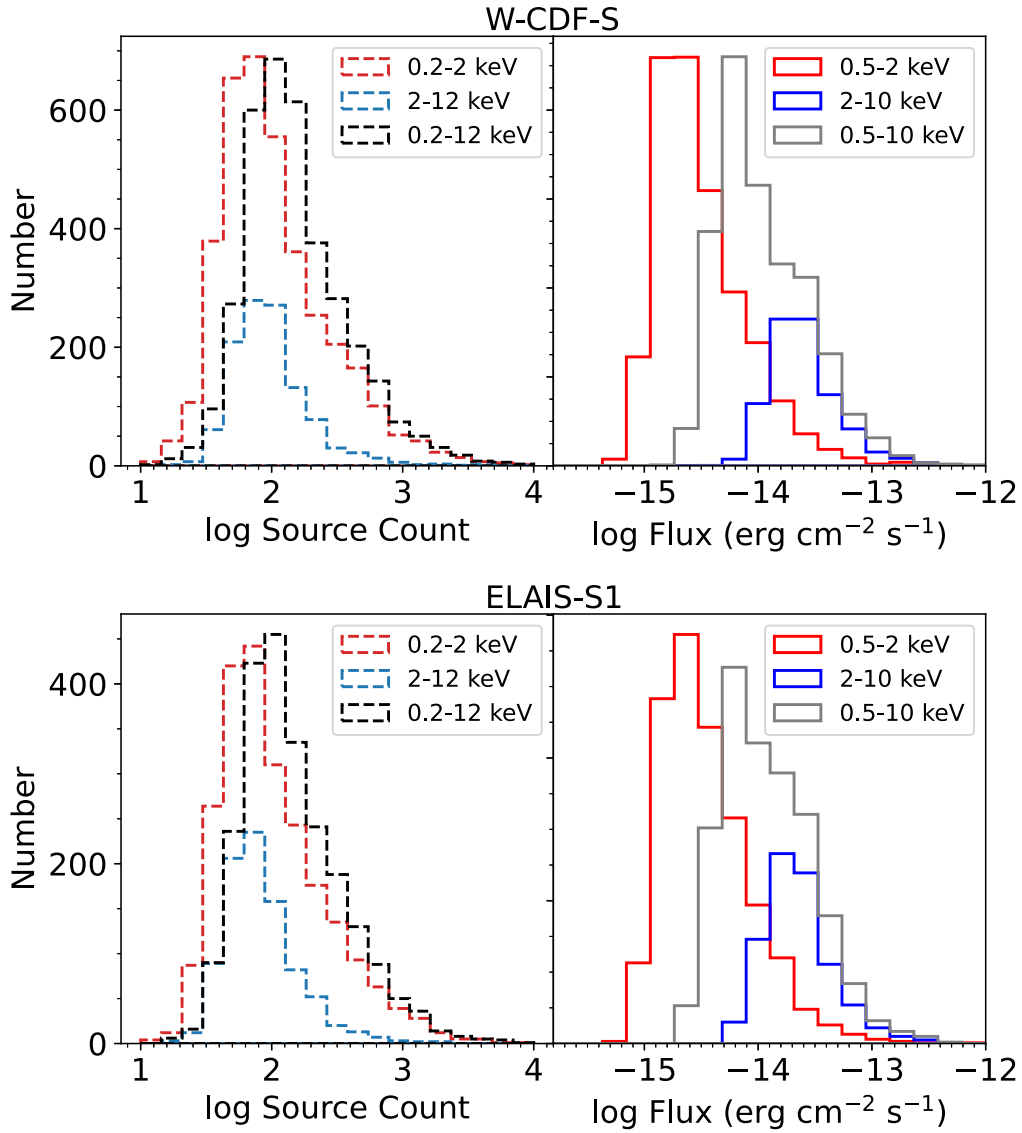

Figure 11. Left panels: the distributions of source counts in the soft (0.2–2 keV; red dashed), hard (2–12 keV; blue dashed), and full (0.2–12 keV; black dashed) bands. Right panels: the distributions of fluxes in the 0.5–2 keV (red), 2–10 keV (blue), and 0.5–10 keV (gray) bands.

by summing all the counts in 5 × 5 pixels of the image centered at the source position, minus all the counts in 5 × 5 pixels of the background map centered at the source position, and then dividing by the EEF. Similarly, for sources that are detected in the hard band but not in the soft band, we stack their soft-band counts at the source positions to obtain a stacked $\Gamma_{\rm eff}$, which is ≈0.6 for both W-CDF-S and ELAIS-S1. When the stacked $\Gamma_{\rm eff}$ value is consistent with the $\Gamma_{\rm eff}$ limit of a source, the stacked $\Gamma_{\rm eff}$ value is utilized to derive the flux; otherwise, the $\Gamma_{\rm eff}$ limit is utilized to derive the flux. When a source is only detected in the full band, $\Gamma_{\rm eff} = 1.4$ (which is approximately the slope of the cosmic X-ray background spectrum; e.g., Marshall et al. 1980) is assumed to derive the flux.

The distributions of source counts in the soft, hard, and full bands and observed fluxes (i.e., fluxes only corrected for Galactic absorption) of the detected sources in the 0.5–2 keV, 2–10 keV, and 0.5–10 keV bands are displayed in Figure 11; we present the observed fluxes in the 0.5–2 keV, 2–10 keV, and 0.5–10 keV bands (calculated with the $\Gamma_{\rm eff}$ values derived in the previous paragraph) to enable direct comparisons with previous X-ray

Table 3
Comparison of Selected Wide-field XMM-Newton Surveys

Field	Area (deg^2)	Depth (ks)	Source Number	Reference
XMM-SERVS	13	30	11925	
SXDS	1.14	40	1245	Ueda et al. (2008)
XMM-COSMOS	2	40	1887	Cappelluti et al. (2009)
XMM-XXL-N	25	10	14168	Chiappetti et al. (2018)
Stripe 82X	31.3	5	6181	LaMassa et al. (2016)

Note. Columns from left to right: survey field, solid-angle coverage, median XMM-Newton PN depth across the field (in kiloseconds), number of sources detected, and example reference for the survey.

surveys (e.g., Cappelluti et al. 2009; Chen et al. 2018). The median observed fluxes of sources in the W-CDF-S field detected in the 0.5–2, 2–10, 0.5–10 keV bands are 5.4×10^{-15}, 1.1×10^{-14}, and 9.0×10^{-15} erg cm^{-2} s^{-1}, respectively. The median observed fluxes of sources in the ELAIS-S1 field detected in the 0.5–2, 2–10, 0.5–10 keV bands are 6.6×10^{-15}, 1.0×10^{-14}, and 1.1×10^{-14} erg cm^{-2} s^{-1}, respectively.

In Table 3, we compare the solid angle and number of detected X-ray sources for the whole XMM-SERVS survey with several other wide-field XMM-Newton surveys, showing the legacy value of XMM-SERVS.

3.6. Survey Sensitivity, Sky Coverage, and log N–log S

We create sensitivity maps in W-CDF-S and ELAIS-S1 in the 0.5–2, 2–10, and 0.5–10 keV bands following the methods in Section 3.6 of Chen et al. (2018). We first bin the mosaicked background and exposure maps in the soft, hard, and full bands for each instrument by 3×3 pixels (which is the bin size recommended by the XMM-SAS task `esensmap`). For each pixel of the binned background map with a background counts number of B, the minimum required source counts (m) for a source to be detected with the `emldetect` detection threshold could be estimated from Equation 3. The sensitivity is calculated with the formula:

$$S = \frac{m - B}{t_{\rm exp} \times {\rm EEF} \times {\rm ECF}}, \quad (5)$$

where energy conversion factors (ECFs) for different bands and different EPIC cameras are derived assuming a power-law spectrum with photon index $\Gamma = 1.4$ modified by Galactic absorption. For X-ray sources in the W-CDF-S field, the adopted ECF values for PN/MOS1/MOS2 are 8.57/2.27/2.28, 1.10/0.38/0.38, and 3.00/0.86/0.87 counts $s^{-1}/10^{-11}$ erg cm^{-2} s^{-1}, when converting count rates detected in the soft band to fluxes in the 0.5–2 keV band, count rates detected in the hard band to fluxes in the 2–10 keV band, and count rates detected in the full band to fluxes in the 0.5–10 keV band, respectively. For X-ray sources in the ELAIS-S1 field, the adopted ECF values for PN/MOS1/MOS2 are 8.03/2.21/2.21, 1.10/0.38/0.38, and 2.78/0.82/0.83 counts $s^{-1}/10^{-11}$ erg cm^{-2} s^{-1}. For each EPIC camera in the soft/hard/full band, we generate a map for the $\frac{1}{t_{\rm exp} \times {\rm EEF} \times {\rm ECF}}$ term in Equation 5, and bin it by 3×3 pixels. As the effective area of PN is ≈2.5 times the effective area of MOS1/MOS2, we combine the $\frac{1}{t_{\rm exp} \times {\rm EEF} \times {\rm ECF}}$ map of PN, MOS1, and MOS2 in each energy band with a weight of 2.5:1:1. Multiplying this merged map with the $m - B$ value at each pixel, we obtain the sensitivity map at 0.5–2/2–10/0.5–10 keV (see Figure 12). Our survey in the W-CDF-S field has flux limits of 1.9×10^{-15}, 2.9×10^{-14}, and 1.0×10^{-14} erg cm^{-2} s^{-1} over 90% of its area in the 0.5–2, 2–10, and 0.5–10 keV bands, respectively. Our survey in the ELAIS-S1 field has flux limits of 2.5×10^{-15}, 3.2×10^{-14}, and 1.3×10^{-14} erg cm^{-2} s^{-1} over 90% of its area in the 0.5–2, 2–10, and 0.5–10 keV bands, respectively. The sensitivity curves corresponding to the DET_ML threshold for the 0.5–2/2–10/0.5–10 keV bands are shown in Figure 13.

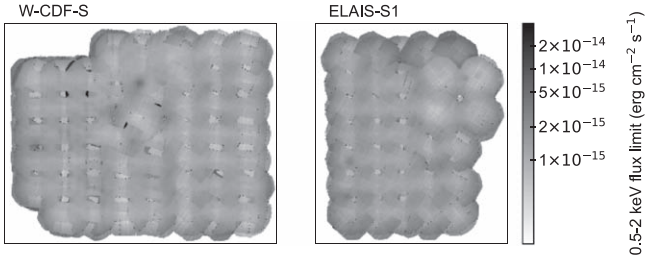

Figure 12. 0.5–2 keV band sensitivity maps in W-CDF-S (left) and ELAIS-S1 (right).

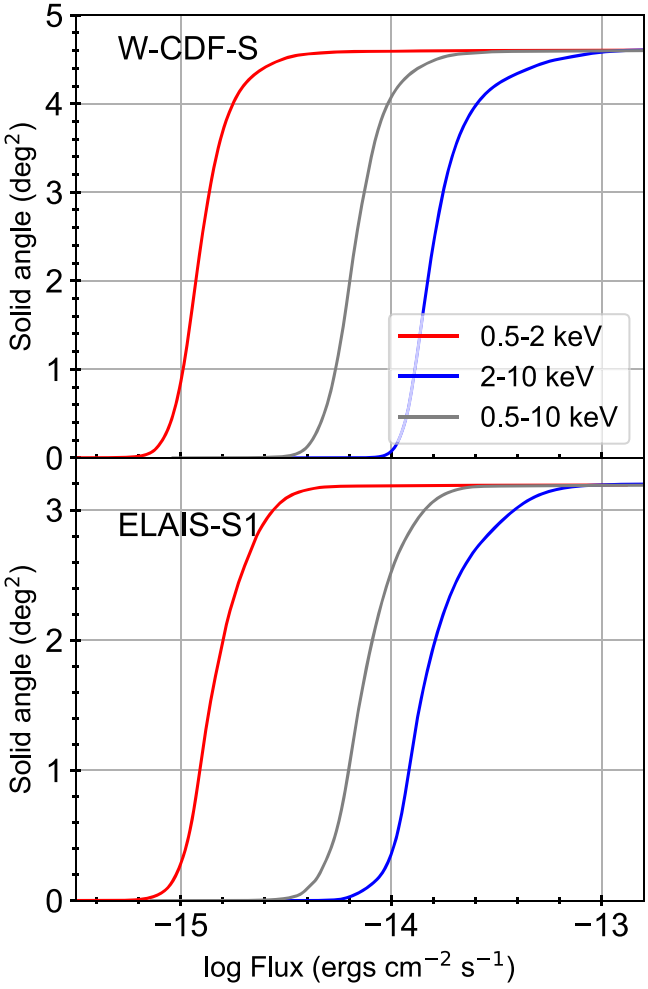

Figure 13. Sensitivity curves in the 0.5–2/2–10/0.5–10 keV band, calculated with the DET_ML thresholds in Section 3.3.

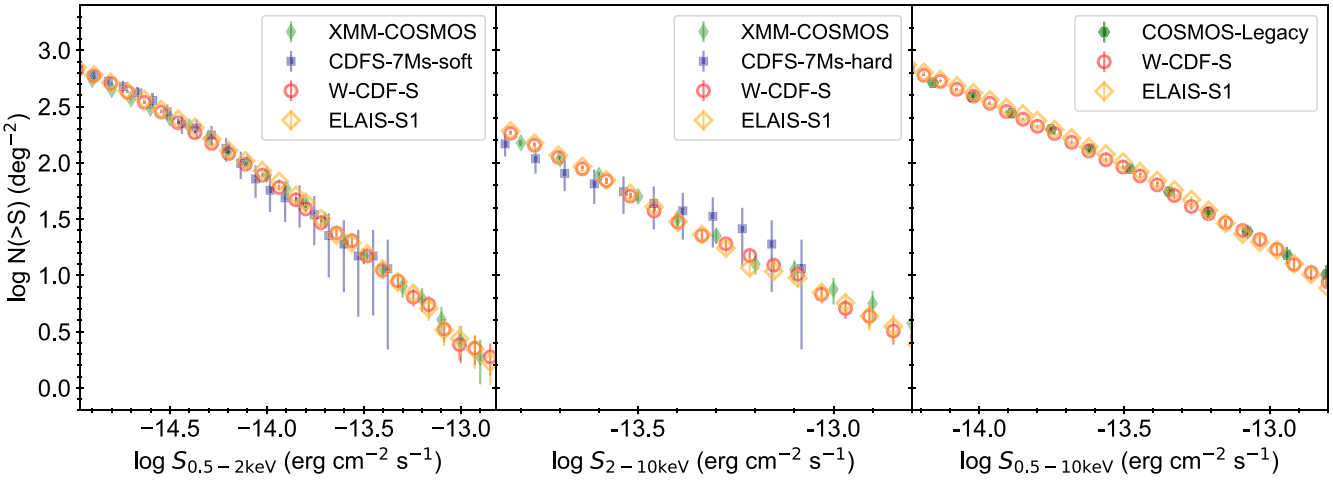

Figure 14. The $\log N - \log S$ relations for our catalogs in the 0.5–2 keV band (left), 2–10 keV band (middle), and 0.5–10 keV band (right). For comparison, $\log N - \log S$ relations from other X-ray surveys are shown (CDF-S 7 Ms, Luo et al. 2017; XMM-COSMOS, Cappelluti et al. 2009; and COSMOS-Legacy, Civano et al. 2016). The $\log N - \log S$ relations of our survey are generally consistent with those of previous studies.

Utilizing these sensitivity curves, we calculate the $\log N - \log S$ relations for our survey (see Figure 14). As can be seen in Figure 14, the $\log N - \log S$ relations in W-CDF-S and ELAIS-S1 are, in general, consistent with the relations reported in other studies (CDF-S 7 Ms, Luo et al. 2017; XMM-COSMOS, Cappelluti et al. 2009; COSMOS-Legacy, Civano et al. 2016; and Stripe 82X, LaMassa et al. 2016) within the measurement uncertainties.

4. Multiwavelength Counterparts of X-Ray Sources

To identify the multiwavelength counterparts for our X-ray sources, we utilize the Bayesian catalog matching tool NWAY (Salvato et al. 2018), which adopts the distance and magnitude/color priors from multiple catalogs simultaneously to select the most probable counterpart, and allows for the absence of counterparts in some catalogs. NWAY has been widely utilized in matching XMM-Newton sources to multiwavelength counterparts (e.g., Chen et al. 2018; Salvato et al. 2018; Liu et al. 2020). Table 3 shows the optical/NIR catalogs utilized in this work. In Sections 4.1 and 4.2, we describe the magnitude/color priors utilized. In Section 4.3, we present the quality of the matched optical/NIR counterparts.

4.1. Obtaining Priors from Chandra Sources

As can be seen from Column 5 of Table 3, it is typical for an XMM-Newton source in our catalogs to have multiple optical/NIR sources located within the 99.73% positional uncertainty ($r_{99\%}$). Thus, to compute the magnitude/color priors of the expected counterparts of our X-ray sources, we make use of the Chandra counterparts of our XMM-Newton sources within the E-CDF-S, CDF-S, and the original $\approx$0.6 deg^2 ELAIS-S1 regions (Feruglio et al. 2008; Xue et al. 2016; Luo et al. 2017), along with other sources reported in the Chandra Source Catalog (CSC) 2.0 (Evans et al. 2010), as Chandra detections have better positional accuracy than XMM-Newton detections. We select Chandra sources that are uniquely matched to sources in our X-ray catalogs within the 95% uncertainties (Chandra and XMM-Newton positional uncertainties are added in quadrature; the positional uncertainties of the Chandra sources are taken from the relevant Chandra catalogs). This approach ensures that the Chandra sources utilized to obtain the priors have similar flux levels as XMM-Newton sources in our catalogs. A total of 264/275 XMM-Newton sources are matched to a unique Chandra counterpart in W-CDF-S/ELAIS-S1. The fluxes and effective power-law indices of matched Chandra sources are in agreement with XMM-Newton sources. Only a small fraction ($\approx$4%) of XMM-Newton sources have >1 Chandra counterpart within the 95% positional uncertainties.

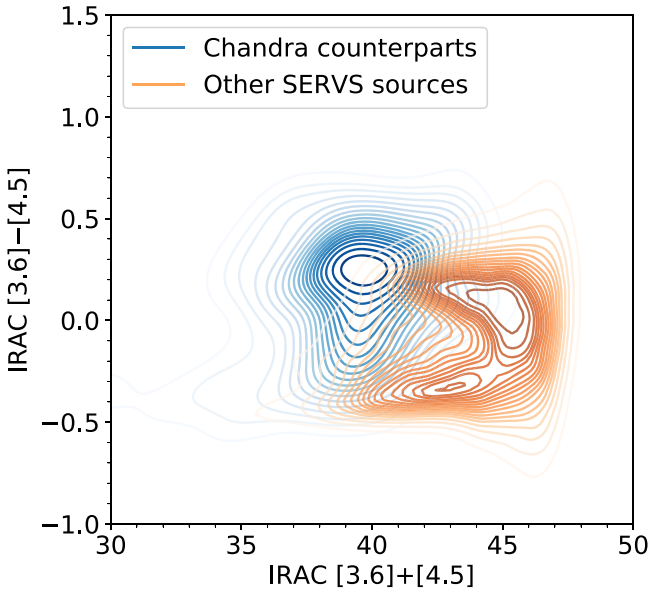

Figure 15. The IRAC [3.6] − [4.5] vs. IRAC [3.6] + [4.5] distribution of sources in the DeepDrill catalog that are matched to Chandra sources (blue contours), and the remaining DeepDrill sources (orange contours). The distribution of DeepDrill sources that have Chandra counterparts shows noticeable differences compared to other DeepDrill sources.

We search for optical/NIR counterparts within 5″ of these Chandra sources with NWAY, utilizing the magnitude priors in the i, K_s, and IRAC 3.6 μm bands generated from the "AUTO" method. We select only reliable counterparts with $p_{\rm any} > 0.8$ (which corresponds to a false-positive fraction of $\approx$5% for Chandra sources; the false-positive fraction is estimated by

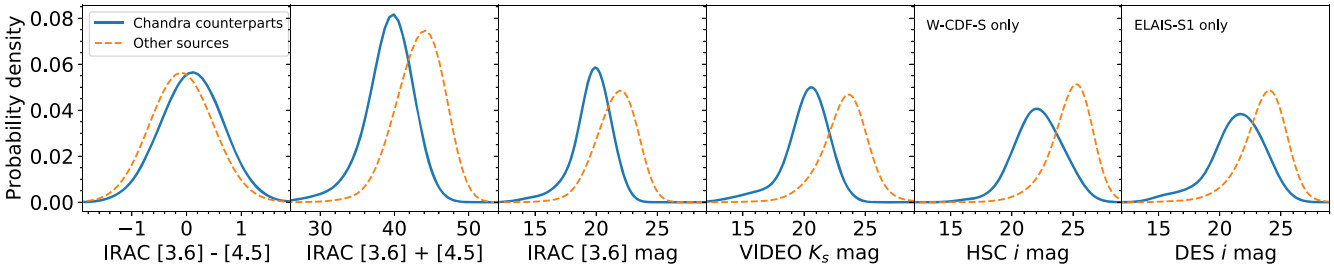

Figure 16. Kernel density estimations of the IRAC 3.6 μm − IRAC 4.5 μm color, IRAC 3.6 μm + IRAC 4.5 μm magnitude, IRAC 3.6 μm magnitude, VIDEO K_s-band magnitude, and HSC/DES i-band magnitude distributions of the expected counterparts of X-ray sources in W-CDF-S and/or ELAIS-S1 (blue solid line) and the unmatched optical/NIR sources in the field (orange dashed line).

Table 4
Summary of Multiwavelength Counterpart-matching Results

Catalog	Limiting Magnitude	Area (deg^2)	σ ($''$)	$\overline{N_{99\%}}$	$f_{matched}$	$f_{reliable}$	f_{FP}	f_{AP} (Simulation)	False Rate (Simulation)	Identical Fraction (Chandra)
(1)	(2)	(3)	(4)	(5)	(6)	(7)	(8)	(9)	(10)	(11)
				W-CDF-S						
DeepDrill	3.6 μm < 23.1	4.6	0.5	1.2	89.6%	85.2%	18.4%	81.0%	4.8%	96.9%
VIDEO	K_s < 23.8	4.5	0.3	2.0	88.3%	82.7%	18.9%	78.8%	5.5%	92.2%
HSC[a]	i < 25.8	4.6	0.1	2.3	95.5%	86.1%	20.8%	82.8%	4.6%	92.6%
Summary	...	...	...	...	100%	88.8%	22.3%	...	...	91.9%
				ELAIS-S1						
DeepDrill	3.6 μm < 23.1	3.2	0.5	1.2	90.5%	84.0%	19.2%	80.4%	4.9%	97.8%
VIDEO	K_s < 23.8	3.0	0.3	2.1	85.1%	76.3%	19.5%	71.0%	7.9%	96.0%
DES	i < 24.6	3.2	0.15	1.5	88.4%	80.8%	20.2%	76.5%	6.3%	97.0%
Summary	...	...	...	...	100%	87.0%	22.4%	...	...	95.2%

Notes. Column 1: Catalog name. Column 2: Magnitude limit. Column 3: Survey area in the XMM-SERVS survey region (4.6 deg^2 for W-CDF-S and 3.2 deg^2 for ELAIS-S1). Column 4: Positional uncertainty adopted for sources in this optical/NIR catalog. Column 5: Average number of sources in this optical/NIR catalog within the 99.73% positional uncertainty ($r_{99\%}$) of the X-ray sources. Column 6: Percentage of X-ray sources with at least one counterpart in this optical/NIR catalog within the 10″search radius. Column 7: Percentage of X-ray sources matched with the optical/NIR catalog that have $p_{any} > 0.1$, which we considered to be reliable matches. Column 8: the fraction of false-positive matches with the optical/NIR catalog among the mock "isolated population" with a p_{any} threshold of 0.1. Column 9: the fraction of X-ray sources in the "associated population" estimated based on simulations. Column 10: False-matching rates for X-ray sources with $p_{any} > 0.1$ estimated from simulations. Column 11: Fraction of the X-ray sources that have identical matching results with the optical/IR catalog when utilizing Chandra or XMM-Newton positions. In the summary row, column 6 represents the percentage of X-ray sources that have at least one of the DeepDrill, VIDEO, or HSC counterparts; column 7 lists the total percentage of X-ray sources that have $p_{any} > 0.1$; column 8 represents the total fraction of false-positive matches among the mock "isolated population"; column 11 contains the fraction of X-ray sources that have identical matched counterparts in all optical and NIR catalogs utilizing Chandra or XMM-Newton positions.

[a] In a small fraction of the W-CDF-S area without HSC coverage (see Figure 1), we add DES sources (Abbott et al. 2021) to the HSC catalog.

matching fake X-ray sources with optical/NIR counterparts; see Section 4.3 for the methods).

As expected from the spectral energy distributions (SEDs) of AGNs, the matched counterparts of Chandra sources occupy a different space in the IRAC [3.6] − [4.5] versus IRAC [3.6] + [4.5] plane compared with other sources in the DeepDrill catalog (see Figure 15). A color and magnitude prior in the NIR has been widely used in the multiwavelength counterpart matching of X-ray sources (e.g., Chen et al. 2018; Liu et al. 2020). Similar to the approach described in Liu et al. (2020), we pixelate the IRAC [3.6] −[4.5] versus IRAC [3.6] + [4.5] space into 50 × 50 pixels, and use a 2D Gaussian kernel estimate to generate the prior ("IRAC 2D prior" hereafter) for the counterparts of X-ray sources in our survey based on the positions of matched Chandra sources/other sources in the DeepDrill catalog on the IRAC [3.6] − [4.5] versus IRAC [3.6] + [4.5] plane. We also compute the 1D IRAC [3.6] − [4.5] and IRAC [3.6] + [4.5] priors utilizing a Gaussian kernel estimate; we compute the magnitude prior for the IRAC 3.6 μm band solely as well (see Figure 16).[46] We do not create VIDEO and HSC (or DES) color priors as done above for the IRAC color, because this action would introduce a bias against type II AGN (just as for most of the VIDEO, HSC, and DES sources that do not have an X-ray counterpart, type II AGNs are typically dominated by host-galaxy light in the optical; e.g., Liu et al. 2020). We do use a Gaussian kernel estimate to obtain magnitude priors for the HSC/DES i band and VIDEO K_s band (see Figure 16).

4.2. Choosing the Priors When Performing Source Matching

Utilizing different combinations of the priors described above, we run NWAY with a maximum distance of 10″ to match

[46] While in Figure 16, DeepDrill sources with/without Chandra counterparts do not seem to have greatly different IRAC [3.6] − [4.5] colors, we note that the peaks of the IRAC [3.6] − [4.5] probability density distributions among these two groups of sources have a difference of ∼0.4 mag, which is roughly consistent with expectation (e.g., see Figure 1 of Stern et al. 2005).

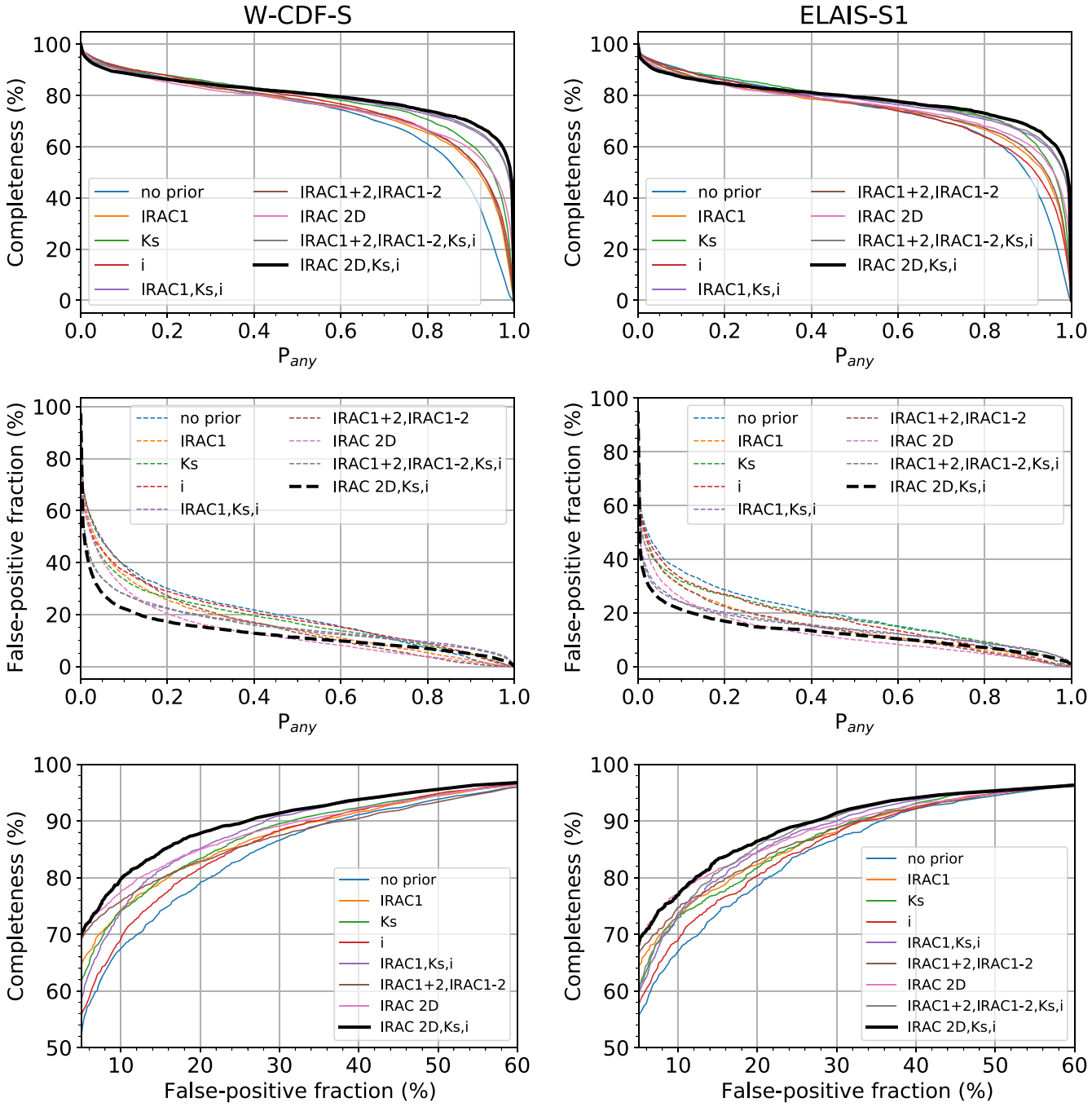

Figure 17. Top: fraction of matched sources above the $p_{\rm any}$ threshold when different priors are adopted. Middle: fraction of matched mock X-ray sources above the $p_{\rm any}$ threshold when different priors are adopted. Bottom: completeness vs. false-positive fraction when different priors are adopted.

detected X-ray sources with the optical/NIR catalogs listed in Table 4. We also generate mock X-ray sources that are 30″ away from any real X-ray sources with NWAY, thus assessing the false-positive fraction of X-ray sources that should not have counterparts (when different combinations of priors are adopted). This false-positive fraction is significantly larger than the expected false rate for the matched counterparts of X-ray sources in the catalog, as most of the actual X-ray sources in our catalog are expected to have optical/NIR counterparts (see Section 4.3 for details).

The completeness for real X-ray sources, and the false-positive fraction among the mock X-ray sources as a function of adopted $p_{\rm any}$ threshold when different combinations of priors are utilized are presented in Figure 17. We also compare the false-positive fraction directly with the completeness when the $p_{\rm any}$ threshold varies. At a given false-positive fraction, combining the following priors: IRAC 2D, i-band mag, and K_s-band mag, yields the highest completeness; at a given completeness, adopting these priors produces the lowest false-positive fraction. Thus, we match XMM-Newton sources with these priors.[47] The percentages of XMM-Newton sources that are matched to each optical/NIR catalog are listed in Table 4, column 6.

[47] We have tested that adding additional magnitude priors from the available optical/NIR bands does not improve the results materially.

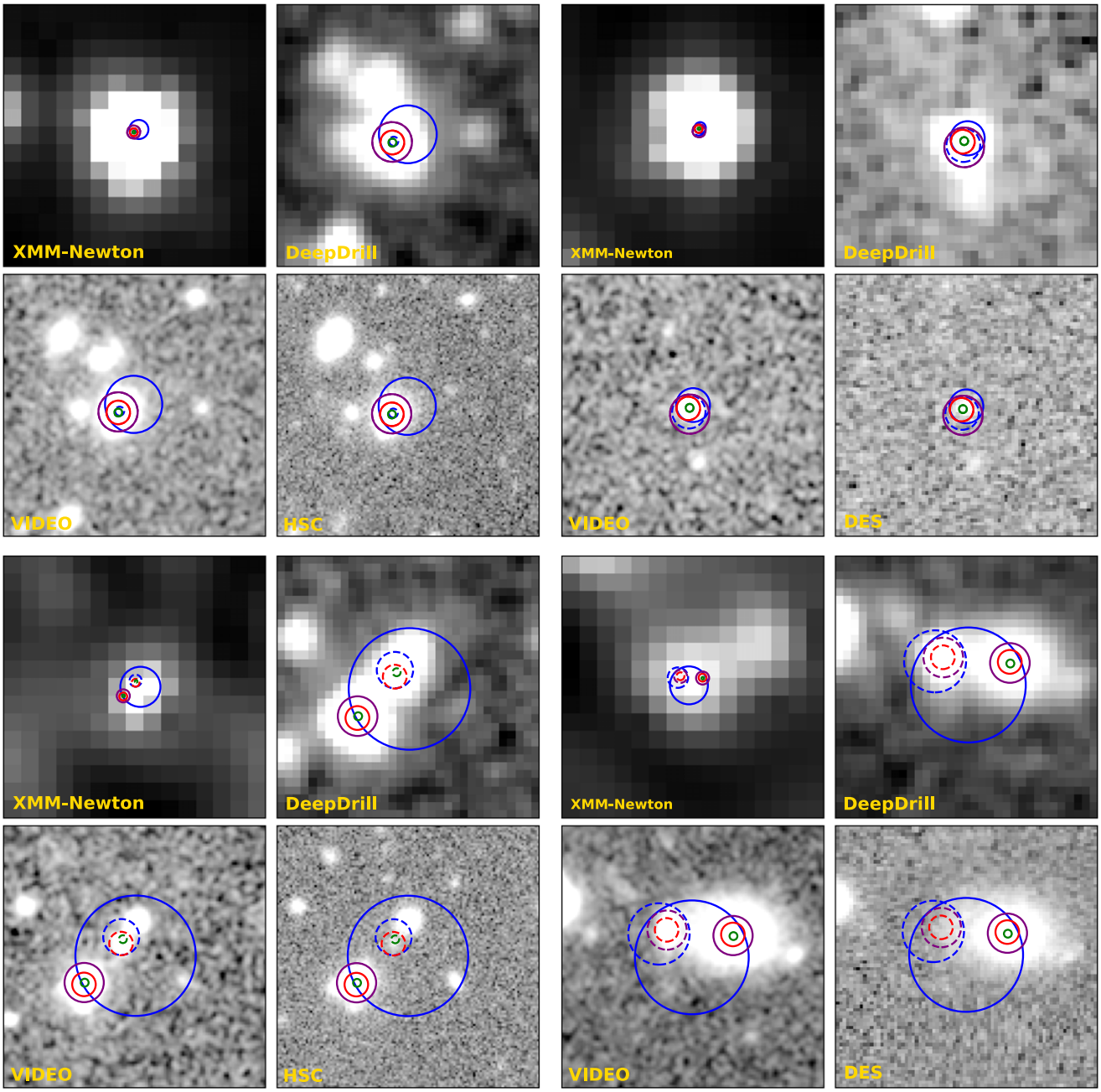

Figure 18. Illustrations of the comparison between the matching results using XMM-Newton positions vs. Chandra positions. Each set of four images shows cutouts from the smoothed XMM-Newton 0.2–12 keV image (top-left; 60″ × 60″), DeepDrill IRAC 3.6 μm band (top-right; 20″ × 20″), VIDEO K_s-band (bottom-left; 20″ × 20″), and HSC *i*-band (for the two W-CDF-S sets on the left) or DES *i*-band (for the two ELAIS-S1 sets on the right) (bottom right; 20″ × 20″). X-ray positions are marked as blue circles with a 99.73% error radius, with the XMM-Newton positions indicated by solid lines and the Chandra positions indicated with dashed lines. DeepDrill counterparts matched utilizing XMM-Newton/Chandra positions are marked with solid/dashed purple circles; VIDEO counterparts are indicated with solid/dashed red circles; HSC/DES counterparts are identified with solid/dashed green circles. In most cases, the counterpart-matching results for XMM-Newton sources are identical to the results obtained using Chandra positions (see the top sets); there is a small fraction of sources where the XMM-Newton results do not agree with Chandra results (see the bottom sets).

4.3. Assessing the Matched Counterparts

The NWAY matching results can be assessed by investigating the subsample of XMM-Newton sources that have matched Chandra counterparts. We compare the matching results of Chandra sources with XMM-Newton sources. For W-CDF-S, the matched DeepDrill counterparts have a ≈97% agreement; the matched VIDEO counterparts have a ≈92% agreement; the matched HSC counterparts have a ≈93% agreement (see column 11 of Table 4). For ELAIS-S1, the matched DeepDrill counterparts have a ≈98% agreement; the matched VIDEO counterparts have a ≈96% agreement; the matched DES counterparts have a ≈97% agreement.[48] Examples of comparisons between the matching results utilizing Chandra and XMM-Newton positions are presented in Figure 18.

[48] The matching results with Chandra or XMM-Newton positions display a slightly higher level of agreement in ELAIS-S1 than in the W-CDF-S, as the XMM-Newton data in the ELAIS-S1 region with Chandra coverage is deeper than the data in the W-CDF-S region with Chandra coverage, leading to better positional accuracy.

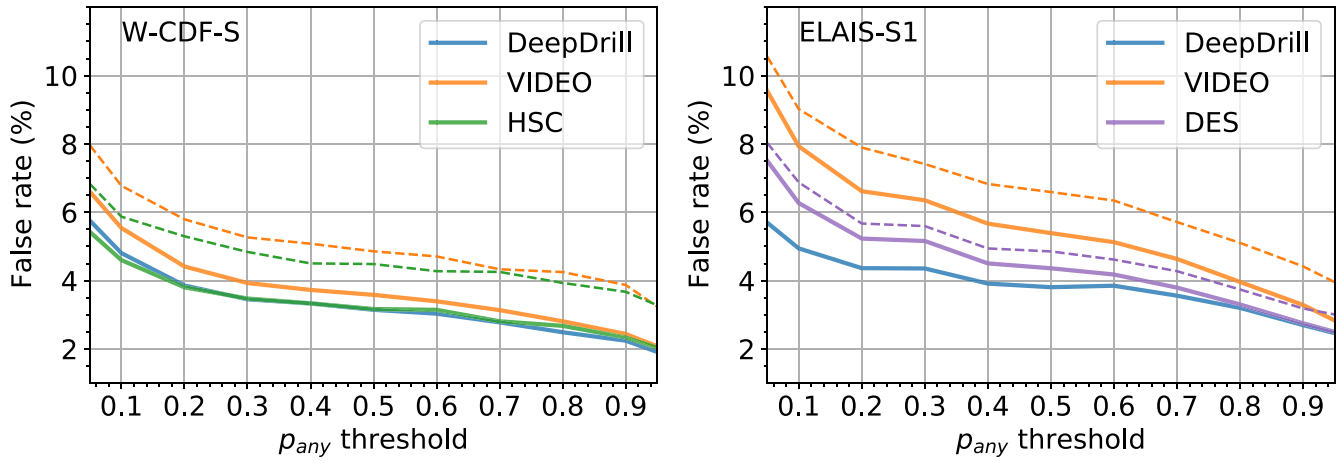

Figure 19. Left: false rate of matched DeepDrill/VIDEO/HSC counterparts as a function of $p_{\rm any}$ threshold adopted (blue/orange/green solid lines) when matching X-ray sources in W-CDF-S to all the optical/IR catalogs simultaneously. The orange/green dashed lines represent the false rates when matching X-ray sources to VIDEO/HSC sources based on their distances to the matched DeepDrill counterparts (when available). Right: false rate of matched DeepDrill/VIDEO/DES counterparts as a function of $p_{\rm any}$ threshold adopted (blue/orange/purple solid lines) when matching X-ray sources in ELAIS-S1 to all the optical/IR catalogs simultaneously. The orange/purple dashed lines represent the false rates when matching X-ray sources to VIDEO/DES sources based on their distances to the matched DeepDrill counterparts (when available).

We have also performed simulations in W-CDF-S and ELAIS-S1, respectively, to assess the results of multiwavelength counterpart matching with NWAY. Following Broos et al. (2011) and Chen et al. (2018), we consider our X-ray sources to have both an "associated population" (X-ray sources that do have a real counterpart in the corresponding optical/NIR catalog) and an "isolated population" (X-ray sources that do not have a real counterpart in the corresponding optical/NIR catalog).

The fraction of the associated population ($f_{\rm AP}$) can be calculated with the formula:

$$N_{\rm negative} = N_{\rm FN} \times f_{\rm AP} + N_{\rm TN} \times (1 - f_{\rm AP}). \quad (6)$$

$N_{\rm negative}$ is the number of real X-ray sources that do not have a matched counterpart in an optical/NIR catalog; $N_{\rm FN}$ is the number of simulated X-ray sources that belong to the "associated population" but do not have a matched counterpart; $N_{\rm TN}$ is the number of mock X-ray sources that belong to the "isolated population" and are not matched to a counterpart as expected. As presented in Section 4.2, NWAY has a built-in function to simulate the isolated population and obtain $N_{\rm TN}$ with varying $p_{\rm any}$ thresholds. To simulate the associated population and calculate $N_{\rm FN}$ with varying $p_{\rm any}$ thresholds, we use a method similar to that in Section 4.2 of Chen et al. (2018). For X-ray sources that have $p_{\rm any}$ values above the adopted $p_{\rm any}$ threshold, we remove all their matched optical/NIR counterparts in the optical/NIR catalogs, and shift the position of all the remaining optical/NIR sources in the catalog by 1′ in a random direction. We then generate fake optical/NIR "counterparts" for each X-ray source based on the X-ray and optical/NIR positional uncertainties, with all the priors utilized. When generating the optical/NIR positions for the W-CDF-S field, we use the positional uncertainty of X-ray sources and HSC sources to simulate HSC positions from the expected Rayleigh distribution of offsets. The generated HSC positions are utilized to simulate the positions of DeepDrill/VIDEO sources, assuming a Gaussian distribution for the offsets between HSC sources with their DeepDrill/VIDEO counterparts (the standard deviation of the Gaussian distribution is derived from all the matched DeepDrill/VIDEO sources with HSC sources within 1″). For the ELAIS-S1 field, DES sources are simulated instead of HSC sources. After that, we run NWAY to obtain $N_{\rm FN}$ among the associated population, thus obtaining $f_{\rm AP}$ by solving Equation 6. With $f_{\rm AP}$, we could obtain the expected false rate ($f_{\rm False}$) of matched counterparts with varying $p_{\rm any}$ thresholds:

$$f_{\rm False} = (N_{\rm IM} \times f_{\rm AP} + N_{\rm FP} \times (1 - f_{\rm AP}))/(N_{\rm positive}). \quad (7)$$

$N_{\rm IM}$ is the number of incorrect matches among the simulated associated X-ray sources; $N_{\rm FP}$ is the number of false positives among the mock isolated X-ray sources. Figure 19 presents $f_{\rm False}$ as a function of the $p_{\rm any}$ threshold adopted. Similar to the finding in Chen et al. (2018), the matched IRAC counterparts have the smallest $f_{\rm False}$ among all the optical/NIR catalogs.

In Section 4.2 of Chen et al. (2018), when SERVS counterparts are available for X-ray sources, other optical/NIR counterparts are selected based on matching them with the matched SERVS counterparts. We also calculate the $f_{\rm False}$ for VIDEO and HSC (or DES) with the following methodology: when an X-ray source has a DeepDrill counterpart, we identify VIDEO and HSC (or DES) counterparts purely based on the distance from the DeepDrill counterpart. The results are presented in Figure 19 as the dashed lines. For VIDEO and HSC (or DES) counterparts, the obtained false rates are slightly higher by ≈1%–2%, revealing the advantages of matching multiple optical/NIR catalogs to XMM-Newton sources simultaneously.

In the released catalogs, we do not apply any $p_{\rm any}$ threshold for the identified multiwavelength counterparts with match_flag = 1 (which indicates that this counterpart is the primary counterpart with the highest likelihood). However, a $p_{\rm any}$ threshold of at least 0.1 is suggested for catalog users so that the false rate of the optical/NIR counterparts is ∼5% (see Table 4, column (10)). A total of 3600/2288 X-ray sources in W-CDF-S/ELAIS-S1 have $p_{\rm any} > 0.1$, which is ≈89%/87% of the total X-ray sources detected (see Table 4, column (7)). For the analyses in Sections 5 and 6 where the optical/NIR counterparts of X-ray sources are utilized, we only use X-ray

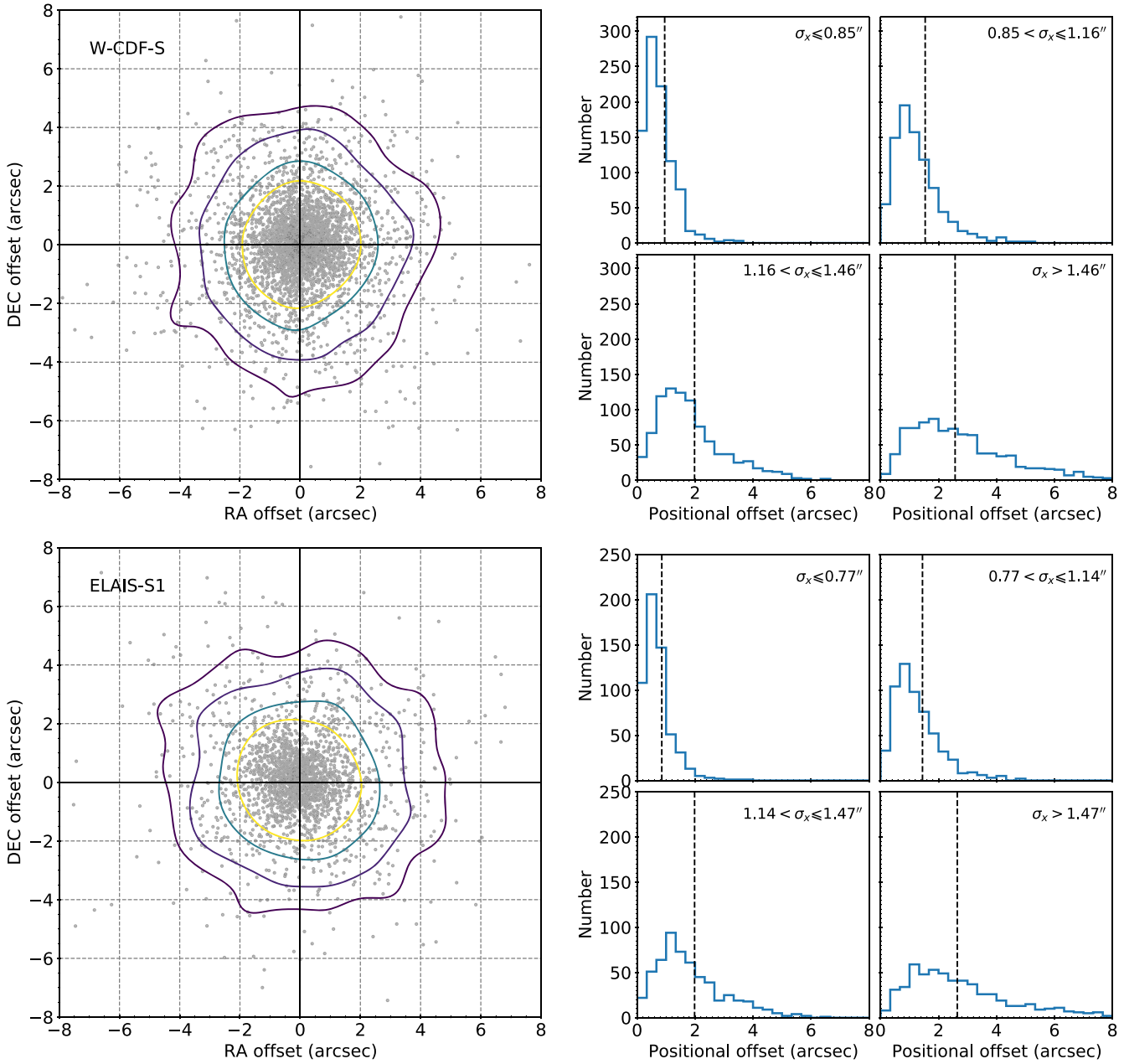

Figure 20. Left: the distribution of decl. offset vs. R.A. offset for X-ray sources in W-CDF-S (top) or ELAIS-S1 (bottom) and their optical/NIR counterparts, with contours indicating the isodensity levels that include 68%, 80%, 90%, and 95% of sources. Right: histograms of positional offsets between X-ray sources in W-CDF-S (top) or ELAIS-S1 (bottom) (which are divided into four bins based on σ_x) and their matched optical/NIR counterparts. The vertical dashed line in each panel represents the median $r_{68\%}$ ($r_{68\%} = 1.515\sigma_x$; see Section 3.4) value in each bin.

sources with $p_{\rm any} > 0.1$ counterparts. Figure 20 displays the offsets between X-ray sources (that have $p_{\rm any} > 0.1$) and their optical/NIR counterparts. Following a priority established based on the survey positional uncertainty, we use the HSC (or DES), VIDEO, or DeepDrill positions as the location of optical/NIR counterparts. Figure 20 also presents histograms of positional offsets when σ_x varies, which demonstrates that our estimation of σ_x from the empirical relation is reliable in general: since $r_{68\%} = \sigma_x \times$ 1.515 (see Section 3.4), we expect the median positional offset in different σ_x bins to increase with σ_x, and roughly 68% of the sources in a given σ_x bin have positional offsets less than the median $r_{68\%}$ in this bin. Compared to many previous XMM-Newton survey catalogs (e.g., Chen et al. 2018; Liu et al. 2020), this work has substantially reduced the X-ray positional uncertainty and decreased the offset between X-ray sources and their optical/NIR counterparts.

5. Redshifts

5.1. Spectroscopic Redshifts

In addition to the extensive photometric data (see Table 1), there are a number of spectroscopic surveys in the W-CDF-S/ELAIS-S1 region (see Table 5).[49] We match X-ray sources to these spectroscopic redshifts (spec-zs) utilizing the positions

[49] There are spectroscopic surveys in the CDF-S/E-CDF-S region that are not listed in Table 5, as we mainly focus on the more relevant wide-area surveys.

Table 5
Spectroscopic Redshift Catalogs Used in This Work, Listed with Priority from High to Low

Catalog	Instrument	Survey Sensitivity	Spectral Resolution	Targeting Fields	Area (deg^2)	$N_{matched}$	$N_{assigned}$	Reference
(1)	(2)	(3)	(4)	(5)	(6)	(7)	(8)	(9)
				W-CDF-S				
OzDES[a]	AAOmega	$r \lesssim 22.5$	~1500	DES-SN C1,C2,C3	9	406	406	Lidman et al. (2020)
ATLAS[a]	AAOmega	$R < 22$	~1300	CDF-S	2.96	155	97	Mao et al. (2012)
BLAST[a]	AAOmega	...	~1300	GOODS-South	3	47	21	Eales et al. (2009)
6dFGS	UKST	$K \lesssim 12.65$	~1000	The Southern Sky	17,000	13	4	Jones et al. (2009)
2dFGRS	AAOmega	$b_J < 19.45$	~800	SGP strip	2000	30	5	Colless et al. (2001)
ACES	IMACS	$R < 24.1$	~750	CDF-S	0.25	80	61	Cooper et al. (2012)
...	VIMOS/DEIMOS	$R < 25$	~180/580	E-CDF-S	0.33	143	70	Silverman et al. (2010)
PRIMUS[a,b]	IMACS	$i \lesssim 23.5$	~30	CDFS-SWIRE,CALIB	2.1	349	252	Coil et al. (2011)
				ELAIS-S1				
OzDES[a]	AAOmega	$r \lesssim 22.5$	~1500	DES-SN E1,E2	6	293	293	Lidman et al. (2020)
ATLAS[a]	AAOmega	$R < 22$	~1300	ELAIS-S1	4.69	46	30	Mao et al. (2012)
6dFGS	UKST	$K \lesssim 12.65$	~1000	The Southern Sky	17,000	10	6	Jones et al. (2009)
2dFGRS	AAOmega	$b_J < 19.45$	~800	SGP strip	2000	5	1	Colless et al. (2001)
...[a]	EFOSC, FORS2	...	>260	ELAIS-S1	0.6	129	106	Feruglio et al. (2008)
...[a]	VIMOS	$R < 24.2$	~210	ELAIS-S1	0.6	134	22	Sacchi et al. (2009)
PRIMUS[a,b]	IMACS	$i \lesssim 23.5$	~30	ELAIS-S1	0.9	223	123	Coil et al. (2011)

Notes. Column (1): redshift survey name. Column (2): survey instrument. Column (3): survey sensitivity. Column (4): spectral resolution. Column (5): targeted fields. Column (6): survey area. Column (7): total number of redshifts matched to the X-ray sources in the catalog. Column (8): total number of redshifts assigned to the X-ray sources in the catalog. Column (9): reference.
[a] Marks redshift surveys where spectroscopic classification for AGNs is available (or partially available).
[b] The low-resolution PRIMUS survey greatly increases the sample with spectroscopic redshifts, although its measurements are not as accurate as other spectroscopic surveys listed and should be used with appropriate caution. For X-ray sources in our catalog, when both spec-z measurements from PRIMUS and those from other high-resolution spectroscopic surveys are available, $\approx 16\%$ of them have $|\Delta z|/(1 + z_{\rm spec,\ high-resolution}) > 0.15$.

of matched optical/NIR counterparts: we search for the nearest spectroscopic redshift position that is within $1''$ of these optical/NIR counterparts. When an X-ray source is matched to multiple spec-zs, we choose redshifts using the priority order in Table 5 (which is ranked based on the spectral resolution, as the accuracy of spec-zs is significantly dependent on the spectral resolution; see note (a) of Table 5 for more details). Most of the spectroscopic surveys in Table 5 have resolution >100. As for the low-resolution PRIMUS survey, we only adopt the $Q \geqslant 3$ (Q is the redshift quality flag provided by Coil et al. 2011) objects. Before matching X-ray sources to the PRIMUS catalog, we utilize the spec-z compilation in the HELP database (Shirley et al. 2019), which provides several additional spec-zs.

In the W-CDF-S catalog, 919 (≈23%) X-ray sources are matched to spec-zs (≈750 of them are outside of the E-CDF-S region), ranging from 0 to 4.56. In the ELAIS-S1 catalog, 585 (≈22%) X-ray sources are matched to spec-zs, ranging from 0 to 4.04 (≈300 of them are outside of the original $\approx 0.6\,deg^2$ ELAIS-S1 region). About 84%/98% of the matched spec-z measurements are from catalogs that have spectroscopic classification for AGNs available in W-CDF-S/ELAIS-S1. Figure 21 shows the distribution of these spec-zs. In the future, there will be more public spectroscopic redshifts from surveys such as CSI (e.g., Kelson et al. 2014), DEVILS (e.g., Davies et al. 2018; Thorne et al. 2021), DESI (e.g., Levi et al. 2019), MOONS (e.g., Maiolino et al. 2020), and WAVES (e.g., Driver et al. 2019).

5.2. Photometric Redshifts

Photometric redshifts (photo-zs) for X-ray sources in this work are derived from SEDs provided by the forced-photometry catalogs in the $4.5/3\,deg^2$ area covered by VIDEO in W-CDF-S/ELAIS-S1 (K. Nyland et al. 2021, in preparation; Zou et al. 2021); these catalogs were generated utilizing *The Tractor* (Lang et al. 2016). *The Tractor* derives consistent flux measurements in all bands with priors of source positions and surface brightness profiles obtained from a fiducial band. As can be seen in Figure 9, most (≈95%) of our X-ray catalog areas are covered by these catalogs. The forced-photometry catalogs are generated following the methods in Nyland et al. (2017), where prior measurements of source positions and surface brightness profiles from a fiducial VIDEO band (which has high resolution) are employed to model and fit the fluxes at other bands. The photometric bands utilized in W-CDF-S include the u, g, r, and i bands in VOICE; g, r, i, and z bands in HSC; Z, Y, J, H, and K_s bands in VIDEO; and 3.6 μm and 4.5 μm bands in DeepDrill (see Table 1 for the survey information). In total, 3319 X-ray sources in W-CDF-S have forced-photometry measurements. For the HSC bands, we only utilize "clean" HSC photometry (see Ni et al. 2019 for details). For a band that is included in two surveys ($g/r/i$), the scatter in two sets of photometry is small (≈0.2 dex), and both detections are utilized in the photo-z calculation. The photometric bands utilized in ELAIS-S1 include the g, r, i, z, and Y bands in DES; B, V, and R bands in ESIS; u band in VOICE; Z, Y, J, H, and K_s bands in VIDEO; and 3.6 μm and 4.5 μm bands in DeepDrill (Zou et al. 2021). In total, 2001 X-ray sources in ELAIS-S1 have forced-photometry measurements. When matching X-ray sources to the forced-photometry catalog, we utilize the position of their matched VIDEO counterparts. Galactic